Variable Fuel Grains Burn Velocities to Reduce Solid-Rocket-Motor Pressure Oscillations

Jérôme Anthoine, Patrick Jézéquel, Michel Prevost, Pierre Prévot, Grégoire Casalis

Variable Fuel Grains Burn Velocities to Reduce Solid-Rocket-Motor Pressure Oscillations

Jérôme Anthoine,* Patrick Jézéquel,† Michel Prévost,‡ and Pierre Prévot§
ONERA–The French Aerospace Lab, 31410 Mauzac, France
and
Grégoire Casalis¶
ONERA–The French Aerospace Lab, 31055 Toulouse, France

Large solid rocket motors are subjected to pressure oscillations for which the origin lies in the coupling between hydrodynamic instabilities and the first longitudinal acoustic modes of the combustion chamber. Static firing tests using two propellant grains in the combustion chamber have been performed. The pressure oscillation amplitude can be strongly modified by varying the burn velocity ratio between the two solid fuel grains. The pressure oscillations are significantly reduced when increasing the burn velocity of the upstream grain and are higher in the opposite case.

I. Introduction

LARGE solid rocket motors (SRMs), such as the U.S. space shuttle redesigned solid rocket motor, the Titan SRM, and the European Ariane 5 P230 moteur à propergol solide, have between three and seven segmented propellant grains, depending on the motor version. Such grain segmentation conducts to low-amplitude but sustained pressure and thrust oscillations, which are present during the second half of operation and appear as discrete bursts for which the frequencies remain close to the first longitudinal acoustic mode ones. The amplitude of these oscillations is not very high (a few 10ths of 1% of the mean pressure but several percent of the mean thrust) but seems to be very sensitive to the environmental conditions. Although such oscillations do not jeopardize the launcher operation, the acoustic mode frequencies are sufficiently low (considering the size of the motors) to possibly introduce coupling phenomena with the launcher's structural modes, and these modes can be consequently transmitted to the payload. Thus, although apparently innocuous, these oscillations have to be controlled.

The oscillations can be induced by unavoidable instabilities that develop in the combustion chamber. Efforts to understand and predict the onset of these oscillations continue to receive attention in the propulsion community [1–3], particularly in the framework of the P230 Programme with the primary booster for the European Ariane 5 launcher [4–7]. For more than 20 years, studies have been carried out in France, especially through the Aerodynamics of Solid Segmented Motors and Pressure Oscillations programs conducted by the Centre National d'Etudes Spatiales (CNES). The main purposes are the identification of the various origins of these instabilities and the understanding of the conditions and the mechanisms of their development [4]. A more recent research and development program (CNES/ONERA–The French Aerospace Lab/Herakles) dedicated to thrust oscillations has allowed us to stress the effects of new parameters and the role of certain couplings between the different phenomena, and finally, to propose practical solutions in order to avoid or at least reduce them. Anthoine [5] recently presented an educational note inspired by the research work conducted jointly by ONERA–The French Aerospace Lab (ONERA) and Herakles under the authority of the CNES.

*Head of Propulsion Laboratory, Aerodynamics and Energetics Modeling Department. Senior Member AIAA.
†Engineer, Aerodynamics and Energetics Modeling Department.
‡Former Head of Propulsion Laboratory, Aerodynamics and Energetics Modeling Department. Senior Member AIAA.
§Research Scientist, Aerodynamics and Energetics Modeling Department.
¶Scientific Deputy Director, Aerodynamics and Energetics Modeling Department. Senior Member AIAA.

II. Earlier Works on Pressure Oscillations

Although resonant combustion and acoustic instabilities such as those studied by Culick [8] and Kuentzmann [9] were originally believed to be the only causes of thrust oscillations, hydrodynamic instabilities of the flow inside the motor have been shown to provide additional sources of perturbations. Hydrodynamic instabilities are caused by unstable flow, featuring vortex-type structures. The first suggestion of acoustic mode excitation by vortex shedding in solid rocket motors was made by Flandro and Jacobs [10], who linked the oscillations to the hydrodynamic instability of the shear regions of the flow and to the coupled response of the motor. Three possible sources of instabilities may be invoked [11]: angle vortex shedding produced by a shear layer created by a chamfered propellant edge; obstacle vortex shedding (OVS) related to the presence of an obstacle such as a frontal thermal protection; and surface (or parietal) Vortex Shedding (SVS), which does not come from a geometric irregularity but results from an intrinsic instability of the internal flow.

The last instability (SVS) can only develop in SRMs with a large L/R aspect ratio. This type of motor can be idealized as a long porous cylinder (without obstacle) in which a Taylor–Culick type of motion may be engendered [12,13]. The resulting bending flow features a natural instability that is potentially capable of generating vortices. This instability, known as velocity coupling [14] in the early 1960s, was first investigated through dedicated hot-gas experiments [15]. This mechanism, called SVS today, has also been identified in different computations [16,17] and through cold-flow experiments [2,17–20].

In parallel, Flandro [21] proposed a theoretical approach based on the vortical/acoustical energy balance, which places the acoustic mode at the core of the phenomenon. More recently, Chedevergne and Casalis [22], Chedevergne et al. [23], Casalis et al. [24] and Chedevergne et al. [25] developed a global approach of the linear stability theory in which the SVS is modeled as a hydrodynamic instability of the flow induced by porous walls in cylindrical ducts. Compared to a local approach, the global one is better adapted to take into account nonparallel effects (namely, the uniform axial acceleration of the average velocity) and to explain the fact that pressure oscillations appear at isolated frequencies, whereas the local approach leads to a continuous branch of amplified frequencies. The incompressible Navier–Stokes equations are normalized by the radial

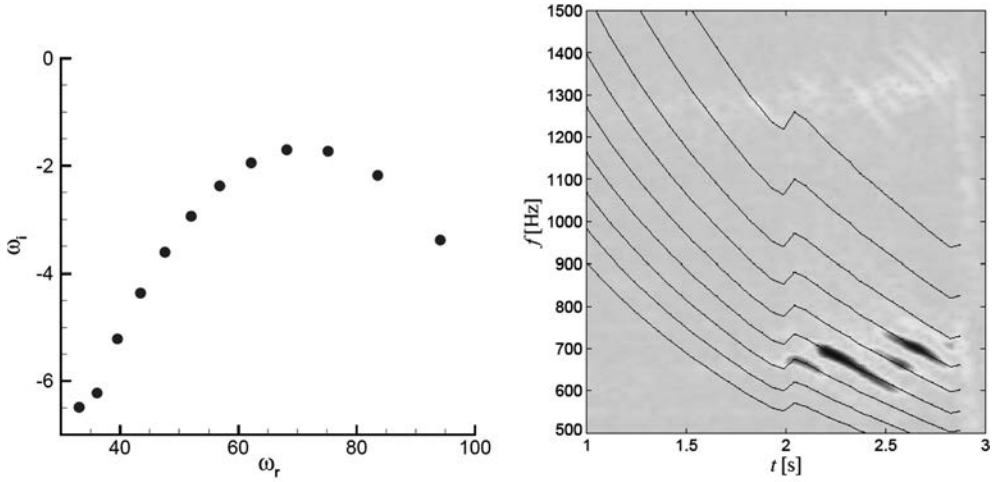

a) Theoretical SVS eigenmodes b) Frequency tracks

Fig. 1 Theoretical SVS eigenmodes [24] and comparison of the measured frequency tracks with recovered theoretical modes for a typical LP9 firing test.

position R of the propellant surface, the mean injection velocity v_{inj}, and the reference time R/v_{inj}. Thus, the aspect ratio L/R and the injection Reynolds number, $Re = v_{\text{inj}}R/\upsilon$, appear as nondimensional parameters that are slightly varying during the firing. It is assumed that the timescale of this variation is much larger than the one of the instability modes. The stability analysis is then performed for different frozen values of Reynolds numbers. Including the boundary conditions, the global linearized Navier–Stokes equations can be written, after discretization, as a matrix generalized eigenvalue problem, $AX = i\omega BX$, where the operators A and B are defined in [24]. The unknown complex eigenvalue is ω, for which the real part ω_r represents the circular frequency of the perturbation and the imaginary part ω_i the temporal growth rate. Negative values of the latter correspond to damped modes, and the less damped branch of dimensionless eigenvalues is plotted in Fig. 1a. Only discrete eigenvalues are obtained, meaning that only discrete (dimensionless) frequencies ω_r are expected to occur. Moreover, all the temporal growth rates ω_i have negative values, indicating that the main flow is stable. On the other hand, a rapid look at the spatial structure of the different eigenmodes shows that each is strongly amplified with respect to the distance from the head end. Thus, if an eigenmode is excited for some reasons (spatial irregularity, acoustic modes, combustion noise, etc.), a coherent structure will be generated downstream induced by the spatial amplification, whereas simultaneously, the mode will be damped with respect to time; the amplitude of the perturbation will decrease up to the occurrence of a new excitation source.

For each firing, it is possible to estimate the temporal evolution of the cylindrical cavity radius R and of the injection velocity v_{inj}. As a consequence, a stability analysis of an equivalent Taylor–Culick base flow, performed at every time, allows for the rescaling of the eigenvalues presented in Fig. 1a with the actual time. For a given stability mode, one obtains a time evolution of the hydrodynamic frequency through the relation $f = (v_{\text{inj}}/2\pi R)\omega_r$. Thus, a discrete set of circular frequencies provides a network of SVS hydrodynamic modes. Each mode of this network has a frequency that evolves during the firing, as shown in Fig. 1b for a typical LP9 firing test. This characteristic evolution is mainly due to the regression (conversely, the radius increase) of the propellant combustion surface during the firing. The theoretical frequency evolutions, represented by solid lines, are compared, in the time-frequency plane, to the frequencies of the pressure oscillations measured at the motor head end. The agreement between the theoretical and the measured frequency paths is very good. It has to be noted that the theoretical network from the biglobal stability theory is calculated independently of the measurements.

Therefore, the measured frequency paths result from the intrinsic instabilities of the mean flow generated by the combustion of the propellant grain (SVS), and these intrinsic instabilities are identified as the primary source of pressure fluctuations [23]. A possible scenario can then be drawn out. For small values of the aspect ratio L/R, the spatial growth of the perturbation is not sufficient to produce large coherent structures. For intermediate values of L/R, these large coherent structures are generated by the instability mechanism. They pass throughout the nozzle, producing across the critical section some perturbations: one being a pressure wave propagating upstream (Fig. 2). This one has been measured in cold-gas setups, and this wave is responsible of the signals measured at the head end of real motors (Fig. 1b). For large values of L/R, the coherent structures are very large and are expected to induce the transition to turbulence, as measured in cold-gas setups [26]. The structures are more or less dissipated by the turbulence so that the amplitude of the coherent structures passing throughout the nozzle may become very small. It can be recalled that, during a real firing, the value of L/R is continuously decreasing so that different regimes may appear successively.

The frequency paths arise around the acoustic modes and, in particular, around the first one (Fig. 1b). It seems reasonable to believe in an interaction between the intrinsic instabilities of the flow and the acoustic modes. When a theoretical mode comes close to an acoustic mode, it is amplified. Then, its frequency moves away from the acoustic one until the following mode has arrived in the vicinity of the acoustic mode. Consequently, a frequency path phenomenon is observed.

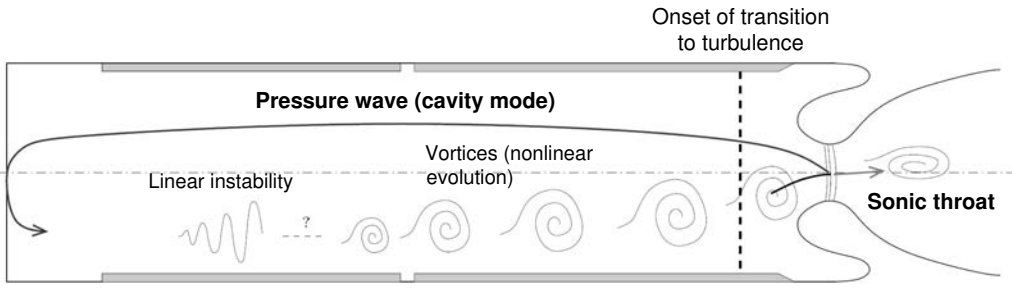

Fig. 2 Proposed physical mechanism of pressure oscillations [23].

The hydrodynamic instabilities are globally damped in time, due to the negative values of ω_i. So, to spark off the observed pressure oscillations, these modes need to be excited. As the frequency ranges of the measured pressure oscillations are always around the axial acoustic modes frequencies, natural acoustics are a possible energy source for the SVS. However, cold-gas experiments have shown that characteristic SVS fluctuations can appear even if the acoustic frequencies differ from the hydrodynamic ones [20]. In this case, the possible energy source is the incoherent noise induced by the wall injection. So, the acoustics (acoustic mode or environmental noise) are only an exciting source for instability modes and is not at the core of the thrust oscillations. Furthermore, the presence of geometrical disturbances can also act as the excitation source of the SVS instability.

So, both acoustic excitation and geometric perturbations yield the appearance of the SVS hydrodynamic instabilities. In actual solid rocket motors, the environmental conditions are rather noisy (combustion noise mainly) and the boundaries are not perfectly smooth (surface of the propellant grains, possible cavities between two consecutive grains, progressive emergence of thermal protections in the flow), so this excitation is unavoidable. In particular, the frontal thermal protection is bent and ablated so that its protrusion is limited. Then, acting more as a source of dispersion with respect to the amplitude of the pressure oscillations, the frontal thermal protection only modifies the SVS instability without generating OVS instability (except for the last bursts of pressure oscillations in which the OVS instability starts to play a role through a coupling with the SVS instability).

Passive control of pressure oscillations remains the only possibility of improving the SRM performance. To limit the pressure oscillations, the goal is to reduce the amplitude and the coherence of the SVS hydrodynamic instability modes. The control of pressure oscillations can then be reached by reducing either the acoustic excitation (i.e., by suppressing the aft-end cavity) or the geometric perturbations [i.e., by using three-dimensional (3-D) geometries] exciting the SVS instabilities. The benefit of suppressing the aft-end cavity was first proved through cold flow experiments [27,28] and then confirmed through hot-gas firing tests [29]. However, in the case of flight engines, removing the cavity has an impact on the thrust vector control system. The use of a 3-D geometry for the frontal thermal protection of the aft propellant grain (referred to as segment S3) provokes a 3-D effect in the internal gas flow that disorganizes the SVS instability [30]. This was first tested using the ONERA LP6 reduced-scale engine with different shapes of the 3-D inhibitor [31]. Then, the most efficient 3-D geometry (at the instant of the third pressure oscillation peak) was evaluated at full scale during a ground firing test [32]. The ripping of the thermal protection makes it difficult to confirm that the reduction in pressure oscillations is really due to the 3-D motif. Moreover, the actual 3-D impact of this thermal protection is not really proved.

Another possibility to reduce the pressure oscillations is to differentiate the propellant compositions of the two last solid fuel grains in order to generate a difference in burn velocity between them. This solution was first tested by the École Nationale Superieure de Mecanique et d'Aerotechnique in a cold-flow test facility with variations of a few percent of the cold-gas velocity ratio between the two grains [33]. Since the result was positive in terms of pressure oscillation reduction, hot-gas firing tests were conducted by ONERA to confirm the reduction in a more representative environment. This solution, at the core of the present paper, is further discussed in Secs. IV and V.

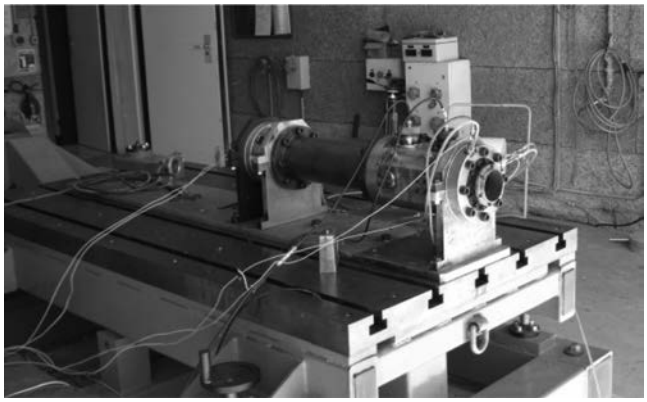

Fig. 3 ONERA LP9 reduced-scale firing test facility before firing.

III. LP9 Firing Test Facility

Large-sized experiments are horrendously expensive, complicated, and time consuming, whereas small-scale models are relatively cheap: their geometry being simpler and modular. However, scaling problems do arise and need to be considered. So, the approach consists of using small-scale motors for precise and well-delimited experiments to deepen the understanding of complicated phenomena such as vortex-shedding-induced pressure oscillations. A thorough knowledge of the basics underlying these instabilities permits us to propose solutions for the reduction of the pressure oscillations. The LP9 firing test facility is an axisymmetric, simplified, and modular engine composed of two grains [7,29]. Figure 3 shows a photograph of the test motor before firing. The LP9 facility has already been used for more than 50 firing tests.

Direct thrust oscillation measurements are very difficult given the scale of these oscillations (about 2% of the overall thrust signal), their frequency, and the mass of the engine. Because it is far easier and more precise to measure chamber pressure, and since thrust oscillations are proportional to pressure oscillations, the LP9 engine is equipped with pressure sensors at both the head end and aft end. The main characteristic of the time evolution of the pressure fluctuations is the existence of frequency paths (Fig. 1b). As it is a time-frequency phenomenon, the unsteady component of the pressure signal is analyzed using a short-time Fourier transform or the Hilbert transform in order to get the time evolution of the pressure fluctuations frequencies. The Hilbert transform [34] consists of tracing the most amplified frequency and its associated amplitude for each time step, using a frequency window around one acoustic mode. The process is applied to the first three acoustic modes.

Besides pressure transducers, ultrasonic sensors are fixed on the fuel grain to measure the radial position of the surface of the propellant at every instant of the firing. The ultrasonic measurement technique has been developed for many years for solid propellant applications [35]. The principle is to emit, from an ultrasonic transducer, a wave that travels through the tested materials, bounces off the regression surface, and comes back to the transducer. Dedicated software calculates the instantaneous regression rate V_b of the solid propellant grain from the travel time of the ultrasonic wave. In the present experiments, this technique allows us to determine the burn velocity ratio.

Table 1 presents the test matrix for the influence of the fuel grain burn velocity ratio. Two different motor configurations are considered, depending on if the nozzle is integrated or not (Fig. 4). For each

Table 1 Static firing test database with different burn velocity ratios between the solid fuel grains

	Configuration 1		Configuration 2	
	Reference test ($V_{b,S2} = V_{b,S3}$): LP9-15		Reference test ($V_{b,S2} = V_{b,S3}$): LP9-15	
Burn velocity ratio	Test case 1 ($V_{b,S2} < V_{b,S3}$)	Test case 2 ($V_{b,S2} > V_{b,S3}$)	Test case 1 ($V_{b,S2} < V_{b,S3}$)	Test case 2 ($V_{b,S2} > V_{b,S3}$)
1.12	— —	— —	LP9-42	LP9-43
1.26	LP9-17	LP9-16	— —	— —

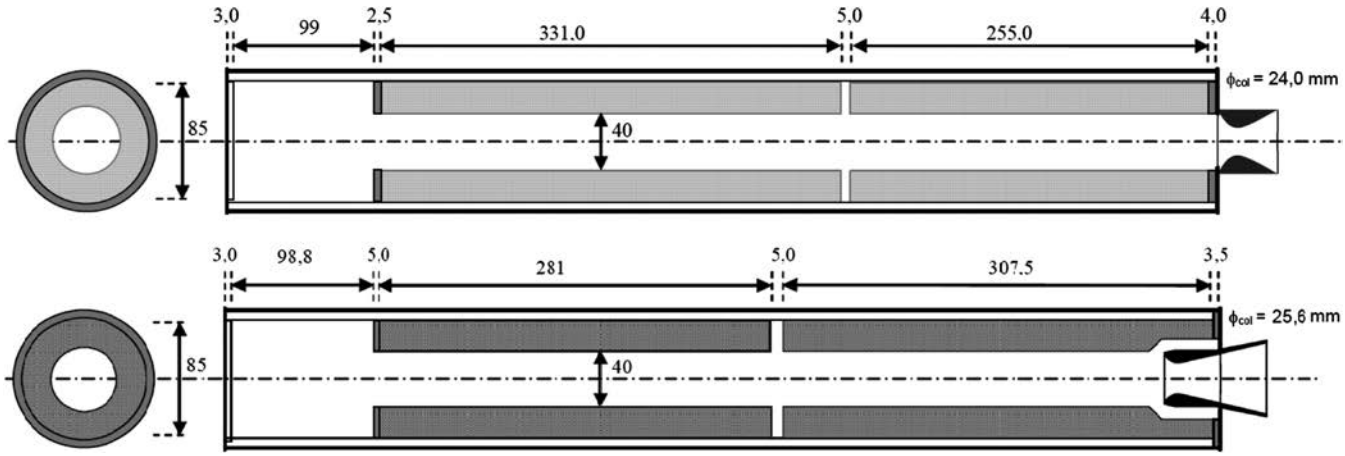

Fig. 4 Sketch of the configurations of the ONERA LP9 reduced-scale firing test facility.

configuration, two different test cases (Fig. 5) are compared to the reference test ($V_{b,S2} = V_{b,S3}$): test case 1 ($V_{b,S2} < V_{b,S3}$) and test case 2 ($V_{b,S2} > V_{b,S3}$). The increased burn velocity of the accelerated composition is obtained either by changing the distribution between the fine and small particles of ammonium perchlorate or by adapting the percentage of catocene. With the fuel compositions being swapped between the test cases (fuel composition of S2 [S3] of test case 1 = fuel composition of S3 [S2] of test case 2), the burn velocity ratios are inversed between test cases 1 and 2.

IV. Test Results for Configuration 1

The first configuration considers an external nozzle without aft-end cavity (Fig. 4, top). The reference test is the LP9-15 (with the nominal propellant composition for both fuel grains). The accelerated composition is obtained by changing the distribution between the fine and small particles of ammonium perchlorate. This composition is used for the S2 grain of the LP9-16 test case and for the S3 grain of the LP9-17 test case, with the other grain of each test case being made out of the nominal composition. Finally, an additional firing test (LP9-18) uses the accelerated composition for both fuel grains.

Figure 6a provides the steady pressure evolutions for the four firing tests. The evolutions from the LP9-16 and LP9-17 firing tests differ from that of the reference test (LP9-15) by pressure levels and burning times, because part of their propellant has a higher regression rate. The LP9-18 firing test has even higher pressure levels, since both grains have a higher regression rate.

To compare the firing tests, the time axis is normalized by the time between the initial pressure rise and the first pressure drop (Fig. 6b). This dimensionless time allows separation of the period during which combustion of both grains occurs ($t_{\text{adim}} < 1$) from the period during which only one grain is still regressing ($t_{\text{adim}} > 1$).

Since the ultrasonic sensors were not yet implemented on the LP9 test facility when these experiments were performed, there is no possibility to get an experimental characterization of the fuel grain burn velocity ratio. This ratio is then deduced using the zero-dimensional simulation tool Vérification Simple de Données Balistiques (VSDB) developed by ONERA. The tool provides the temporal evolution of the steady pressure $P(t)$:

$$P(t) = \sqrt[(1-n)]{\rho_p a \lambda H(t) \eta c^*_{\text{th}} \frac{S_p(t)}{A_{\text{col}}(t)}} \tag{1}$$

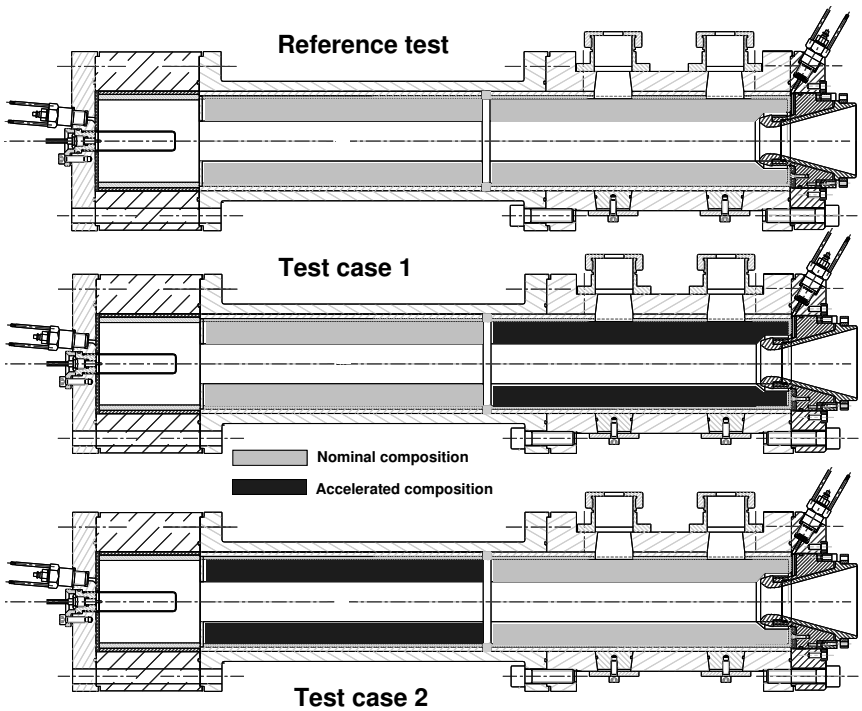

Fig. 5 Different test cases of the LP9 facility for the burn velocity ratio database (configuration 2).

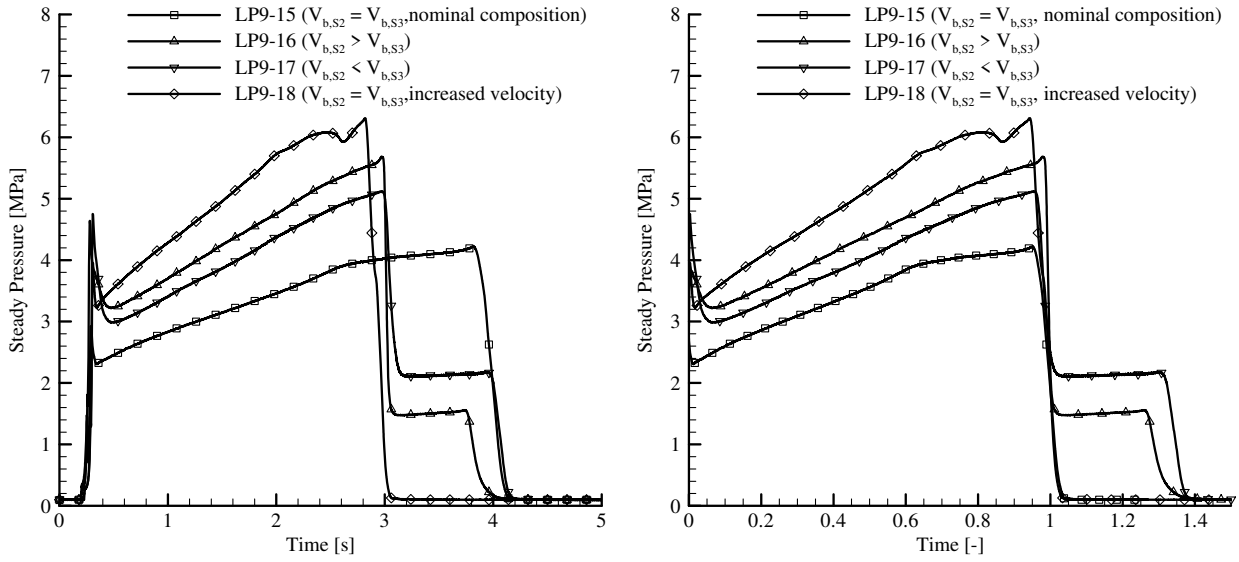

a) Dimensional time **b) Nondimensional time**

Fig. 6 Steady pressure evolution for configuration 1 with burn velocity ratio of 1.26.

where a and n are the coefficients of the regression rate law $V_b(t) = a[P(t)]^n$, ρ_p is the propellant density, c^*_{th} is the theoretical characteristic velocity, $S_p(t)$ is the combustion surface, and $A_{\text{col}}(t)$ is the nozzle throat section. The scale effect coefficient λ and the hump effect $H(t)$ modify the a coefficient, whereas the combustion efficiency η influences the theoretical characteristic velocity.

The VSDB code operated initially with the burnt thickness as a variable. This procedure based on a predefined burned thickness step assumed that the propellant composition was the same for all the grains and that they burned at the same rate, which does not allow simulating grains with different burn velocities. VSDB has been modified so that the calculation progresses according to a predefined time step. At each time step, the program calculates the burned thickness of each grain on the basis of the regression rate of the grain determined in the preceding time step. The burned thickness can thus be different, depending on the fuel grain. Then, the program calculates the combustion surface of each grain S_{Si} from the load geometric data and the stationary pressure is obtained by the following formula:

$$P(t) = \sqrt[(1-n_{\text{moy}})]{\rho_{p,S1} a_{S1} \lambda_{S1} H_{S1}(t) \eta_{S1} c^*_{\text{th},S1} \frac{S_{S1}(t)}{A_{\text{col}}(t)} + \rho_{p,S2} a_{S2} \lambda_{S2} H_{S2}(t) \eta_{S2} c^*_{\text{th},S2} \frac{S_{S2}(t)}{A_{\text{col}}(t)} + \ldots} \tag{2}$$

The regression rate of each grain is then calculated by the formula $V_{b,Si}(t) = a_{Si}\lambda_{Si}H_{Si}(t)[P(t)]^{n_{\text{moy}}}$, which finally gives the burned thickness at the next time step. The initialization is done with the initial combustion surface of the different grains.

The LP9-15 (nominal propellant) and LP9-18 (increased burn velocity) firing tests are used to calibrate the parameters of the VSDB tool for each propellant composition. These parameters are provided in Table 2, and the comparison between the calculated steady pressure evolution and the experimental data is shown in Fig. 7a. The VSDB tool is then applied, with the same parameters (Table 2), to the LP9-16 and LP9-17 firing tests. There is a good match between the calculated and the experimental data for both firing tests (Fig. 7b), indicating that the burn velocity ratio between the grains is equal to 1.26 (from Table 2).

Figure 8 shows the Hilbert transform of the unsteady pressure signals around the first longitudinal acoustic mode frequency. The unsteady pressure amplitude is normalized by the P_{ce} conventional value, the time by the same procedure as mentioned before, and the frequency by the first longitudinal acoustic mode frequency. A significant reduction of pressure oscillations is observed for the LP9-16 test compared to the reference test (LP9-15), and the instabilities are no longer organized in the frequency domain. On the other hand, the instability amplitudes for the other test (LP9-17) remain similar to those of the reference test for the first time period (for $t_{\text{adim}} < 1$) and are still associated to frequency paths. When only combustion of the S2 grain remains ($t_{\text{adim}} > 1$), an instability with a very high amplitude is observed and its time evolution presents two long frequency paths. It could be associated with the presence of a large cavity without flow injection in the rear part of the engine.

The steady pressure evolutions for the LP9-16 and LP9-17 firing tests differ too much from the pressure evolution of the reference test to be useful in a flight engine. It follows that the burn velocity ratio of 1.26 is too high to consider implementing this solution on a full-scale solid rocket motor. A more realistic burn velocity ratio of 1.12 has been tested in configuration 2 with an integrated nozzle.

Table 2 VSDB parameters for modeling the steady pressure evolution of firing tests LP9-15 and LP9-18

	Nominal propellant composition	Increased burned velocity composition
Regression rate	6.4 mm/s (at 4.5 MPa)	8.1 mm/s (at 4.5 MPa)
Exponent of regression rate law n	0.22	0.22
Combustion efficiency η, %	98	98
Scale effect coefficient λ	1.035	1.035

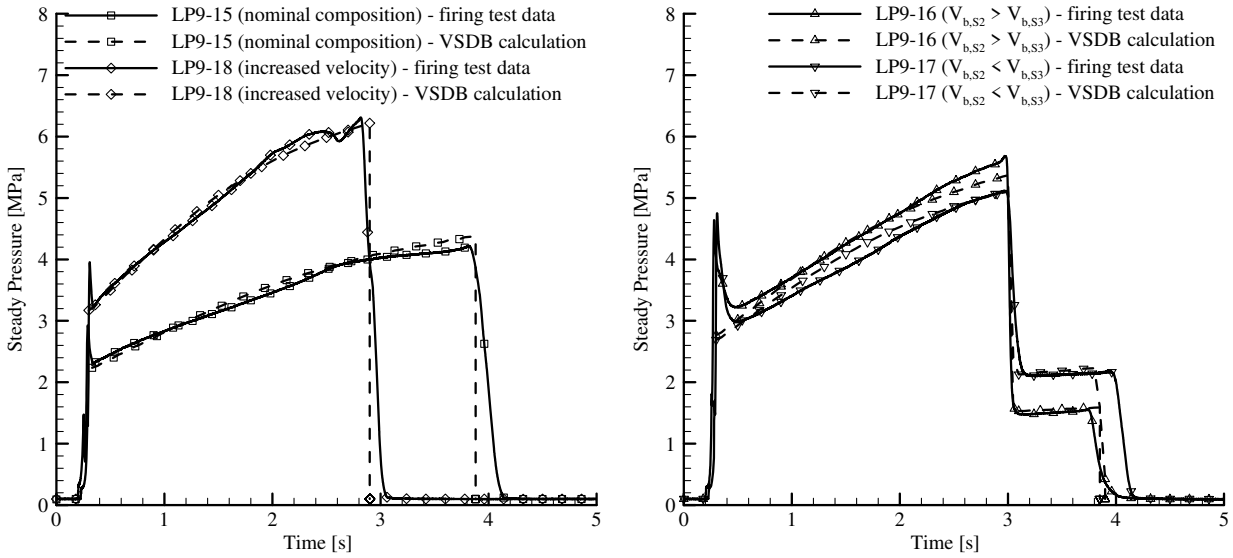

a) LP9-15 and LP9-18 **b) LP9-16 and LP9-17**

Fig. 7 VSDB modeling of the steady pressure evolution of firing tests LP9-15 to LP9-18.

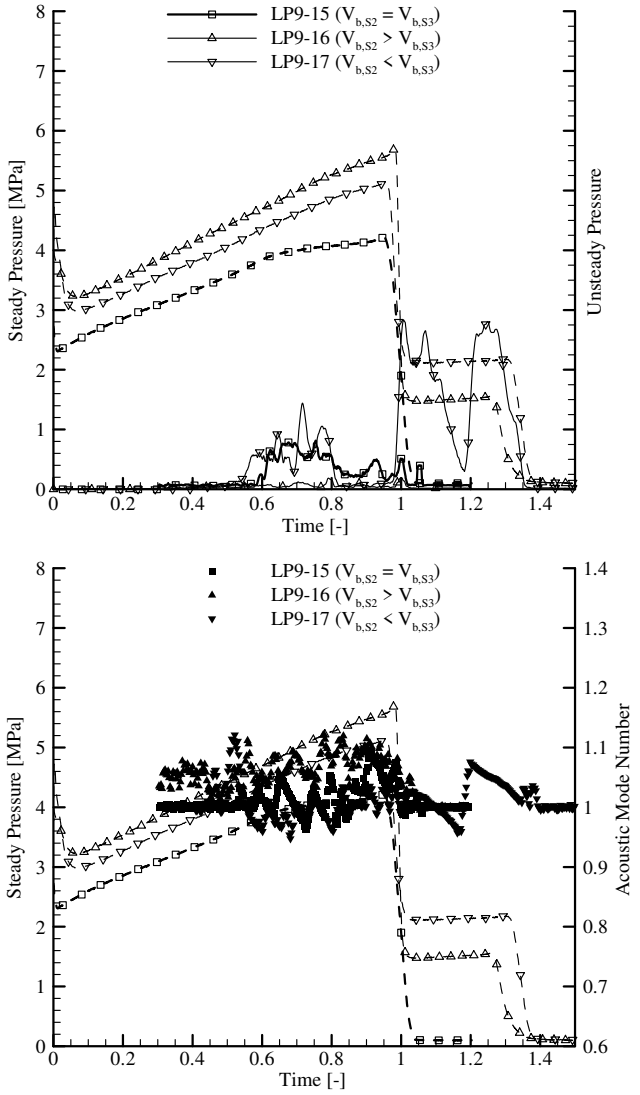

Fig. 8 Hilbert transform on the first longitudinal acoustic mode of the unsteady pressure signals for configuration 1 with a burn velocity ratio of 1.26.

V. Test Results for Configuration 2

The reference test of configuration 2 (LP9-24 firing test) has an interblock cavity, an aft-end cavity, and a submerged nozzle. The propellant composition for the two blocks of this reference test is a Butalite with 3% of catocen. The burn velocity ratio is obtained by combining one grain of this composition with another grain from a Butalite with 4.6% of catocene. The value of the burn velocity ratio is deduced from the application of the ultrasonic measurement technique.

Figure 9 provides the time evolutions of the propellant thicknesses measured by the ultrasonic sensors located along grains S2 and S3 for the LP9-43 firing test. Deduced regression rates are also plotted in Fig. 9. The propellant regression rate at 4.5 MPa is computed as the average value of the ultrasonic sensor measurements when the steady pressure is between 4 and 5 MPa. It is equal to 10.6 mm/s for the S2 grain with the accelerated propellant composition (4.6% of catocene) and equal to 9.5 mm/s for the S3 grain with the nominal propellant composition (3% of catocene). Based on these values, the burn velocity ratio ($V_{b,S2}/V_{b,S3}$) is equal to 1.12.

Figure 10 shows the steady pressure evolution for configuration 2 with a burn velocity ratio of 1.12. The evolutions from the LP9-42 and LP9-43 firing tests differ from that of the reference test (LP9-24) by pressure amplitudes and burning times, for the same reason as before. A different evolution of the steady pressure is observed when the rear end cavity has fully burned. The corresponding dimensional time appears earlier for the LP9-43 firing compared to the reference test, given that the average operating pressure is higher for that test, resulting in a higher overall regression rate. The full burning of the rear end cavity for the LP9-42 test happens even earlier, although the operating pressure is close to that of the LP9-43 test, due to the accelerated composition of the S3 grain.

Figure 11a shows the result of the Fourier transform based on the analysis of the complete unsteady pressure signal. The frequency is normalized by the first longitudinal acoustic mode frequency. All three tests have peaks at the same frequencies associated to the three first longitudinal acoustic modes, and the bandwidths of the three modes are the same. The LP9-43 firing test is associated with extremely low-amplitude levels, especially for the first acoustic mode. The signal of the LP9-42 firing test is less attenuated at the first acoustic mode and is even largely amplified at the second acoustic mode.

The comparison of the temporal evolutions of the maximum rms amplitude of the unsteady pressure signals within the first acoustic mode bandwidth is given in Fig. 11b. The unsteady pressure amplitude is normalized by the P_{ce} conventional value. A very significant reduction of instability amplitudes is observed for the LP9-43 test,

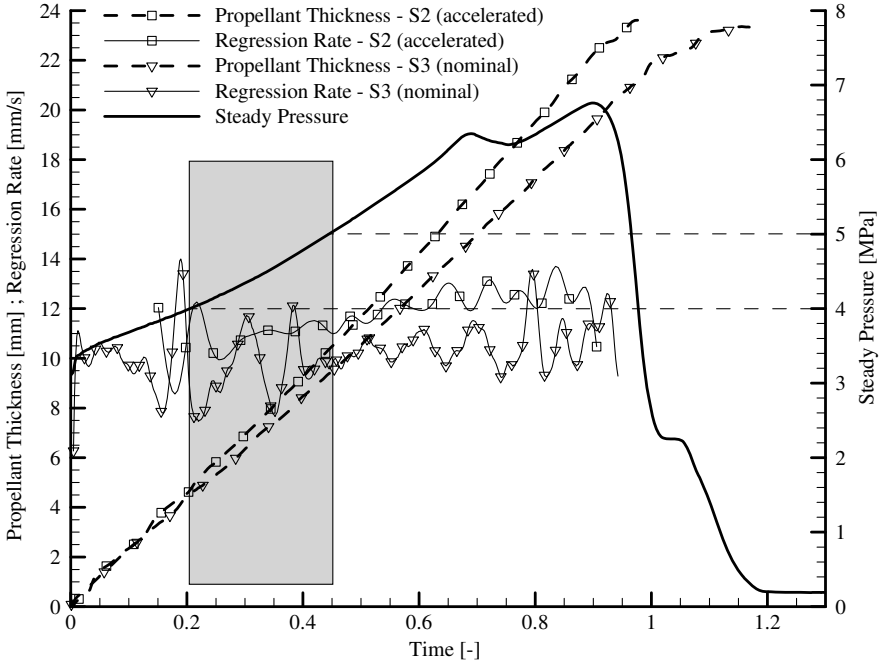

Fig. 9 Instantaneous evolutions of the propellant regression rates measured with the ultrasonic sensors during the LP9-43 firing test.

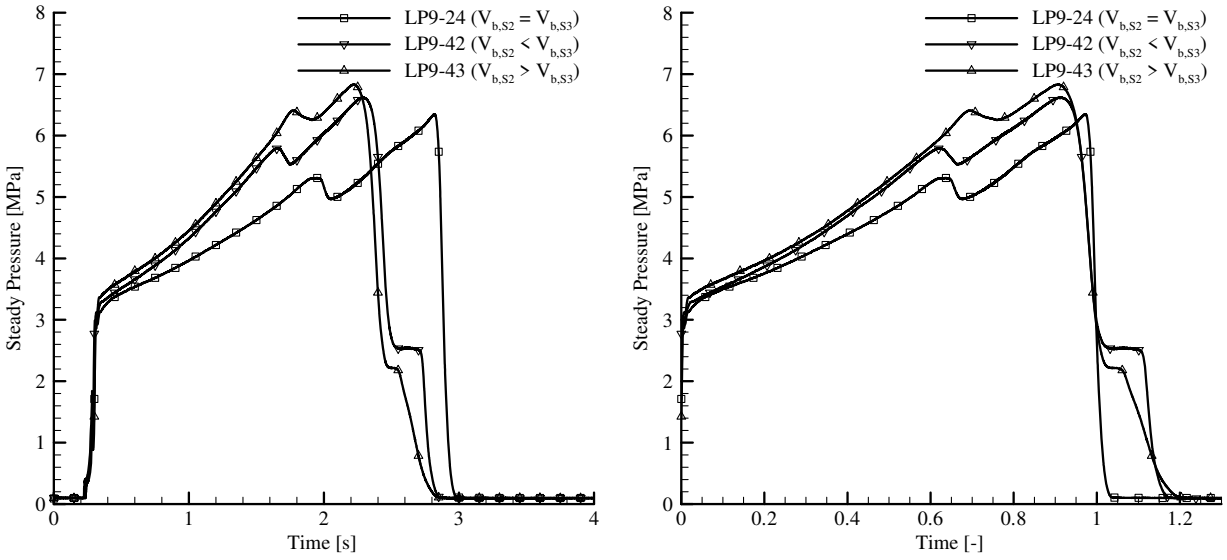

a) Dimensional time **b) Nondimensional time**

Fig. 10 Steady pressure evolution for configuration 2 with a burn velocity ratio of 1.12.

with the maximum amplitude being reduced by a factor of six. On the other hand, significant instabilities are still observed for the other test (LP9-42) and are comparable to the instability amplitudes of the reference test for the first time period (for $t_{adim} < 1$). When only combustion of the S2 grain remains ($t_{adim} > 1$), another high-level instability is observed, similar to the one observed before (LP9-17 test).

Figure 12a shows the Hilbert transform of the unsteady pressure signals around the first longitudinal acoustic mode frequency. The instability levels are slightly higher for the LP9-42 test compared to the reference test, whereas the LP9-43 test shows a large decrease of the pressure oscillations that are no longer organized in the frequency domain. The new instability is again clearly observed for the LP9-42 test when the S3 grain is completely burned (for $t_{admin} > 1$). This instability is characterized by a frequency shift different from that observed for the other bursts and other firing tests featuring pressure oscillations of the SVS type. It confirms that the underlying hydrodynamic phenomenon is certainly of a different type and could be due to the presence of a large cavity without flow injection at the rear part of the engine.

The Hilbert transforms of the unsteady pressure signals around the second longitudinal acoustic mode frequency are compared in Fig. 12b. The pressure oscillations have increased for the LP9-42 test, whereas the LP9-43 test only shows very weak instabilities that are unorganized in frequency.

The previous observations are also confirmed through the application of the HRogram method (Fig. 13). This method is based on a least-squares algorithm to decompose sounds into sines-plus-residual models and allows computation of the slowly varying time-dependent amplitudes and frequencies of a definite number of distinct spectral components [36]. The significant reduction in pressure oscillations through the use of fuel grains with different burn

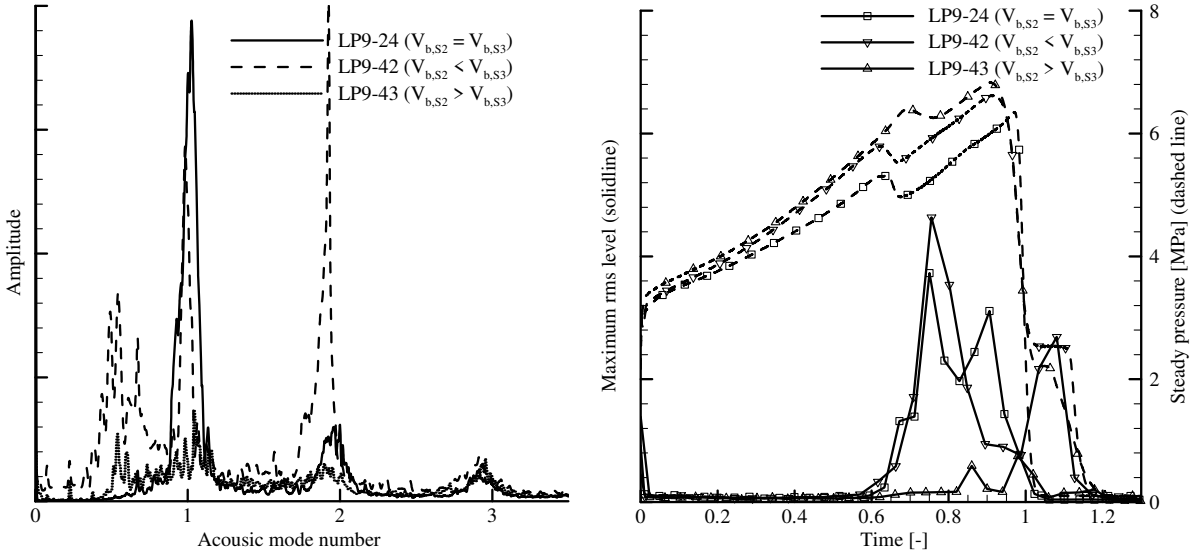

a) Fourier transform **b) Maximum rms level around the first acoustic mode**

Fig. 11 Unsteady pressure signals for configuration 2 with a burn velocity ratio of 1.12.

velocities has been proved. However, the pressure oscillations are significantly reduced in amplitude and become unorganized in frequency only when the S2 grain burns faster than the S3 grain (LP9-43 firing test). Otherwise, pressure oscillations are even slightly increased with a shift to the second longitudinal acoustic mode, and a new instability appears when only combustion of the S2 grain remains.

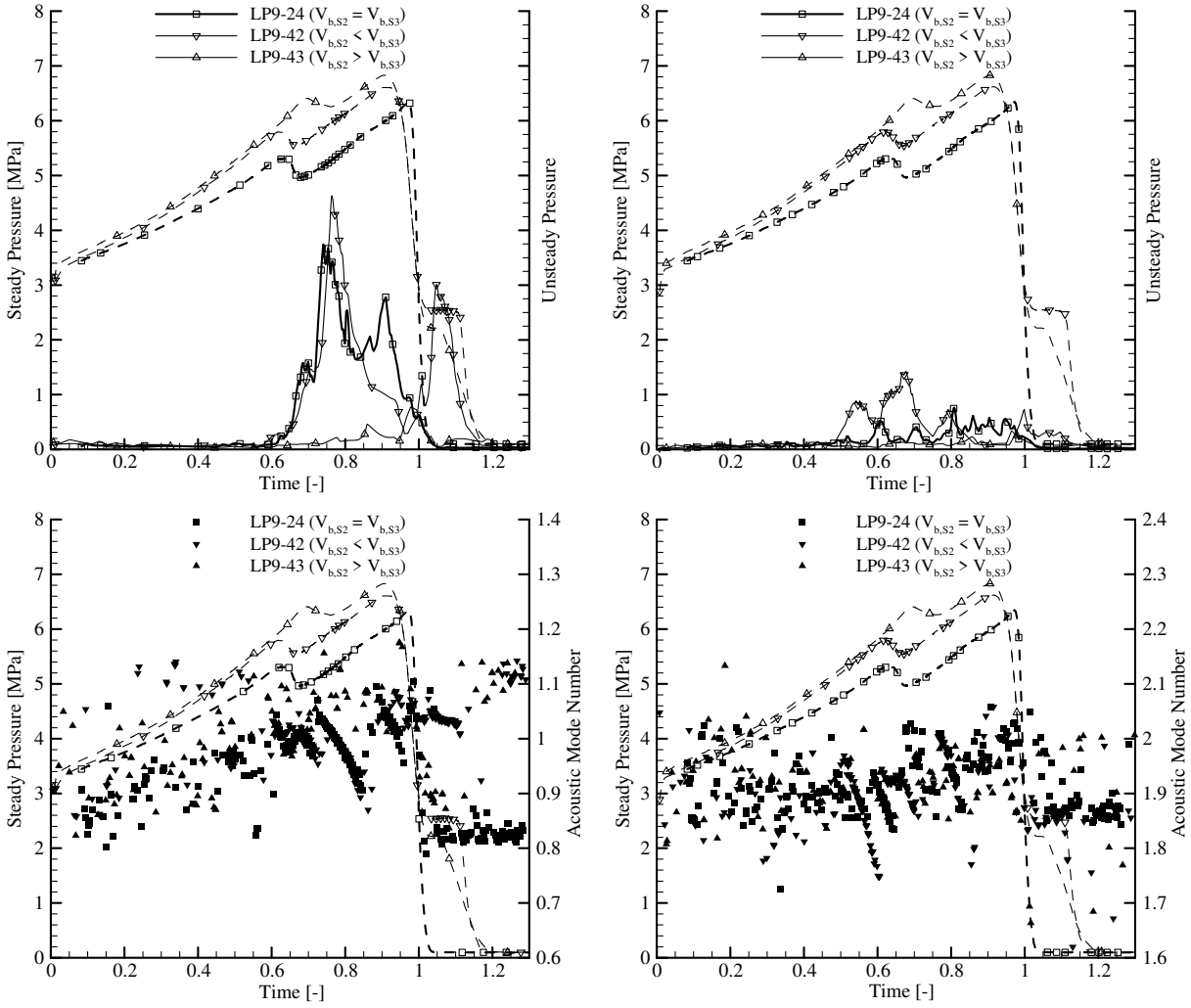

a) First longitudinal acoustic mode **b) Second longitudinal acoustic mode**

Fig. 12 Hilbert transforms of the unsteady pressure signals for configuration 2 with a burn velocity ratio of 1.12.

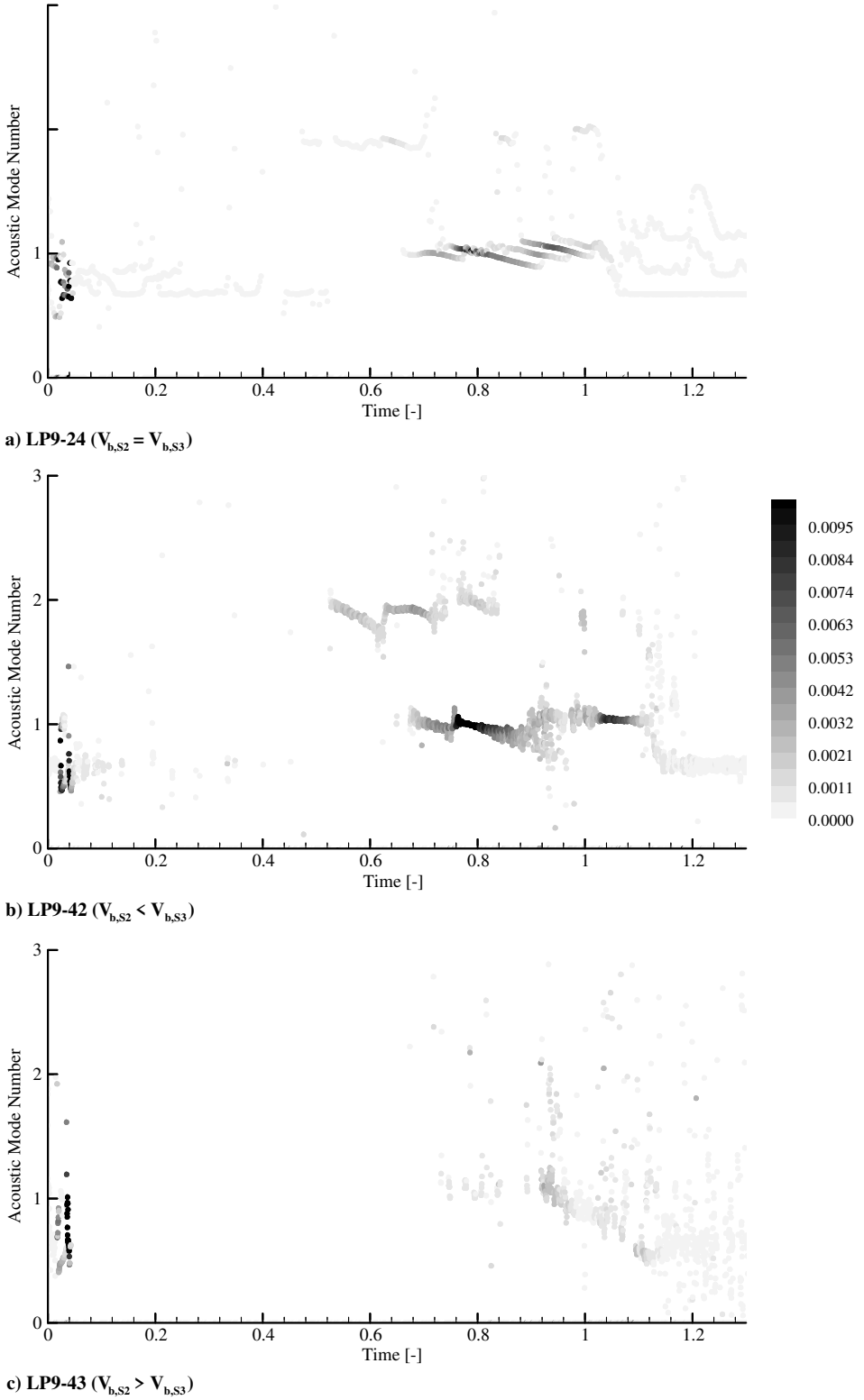

a) LP9-24 ($V_{b,S2} = V_{b,S3}$)

b) LP9-42 ($V_{b,S2} < V_{b,S3}$)

c) LP9-43 ($V_{b,S2} > V_{b,S3}$)

Fig. 13 HRogram method applied to the unsteady pressure signals for configuration 2 with a burn velocity ratio of 1.12.

VI. Conclusions

An important reduction of pressure oscillations is clearly demonstrated when introducing a burn velocity ratio between the two fuel grains. However, reduction is only observed when the burn velocity of the upstream grain is higher than that of the downstream one ($V_{b,S2} > V_{b,S3}$). Compared to the reference test case, the increase of the burn velocity of the upstream propellant grain significantly reduces the pressure oscillations, and the instabilities are no longer organized along frequency paths. This has been proved for a large burn velocity ratio, which is not applicable to a full-scale SRM but is also for the moderate burn velocity ratio of 1.12. These results have been obtained with the LP9 firing test facility.

In the opposite case (when $V_{b,S3} > V_{b,S2}$), the pressure oscillations are even slightly amplified and an instability appears when the S3 grain is completely burned and only combustion of the S2 grain remains. This instability is characterized by a frequency shift different from those observed for the other bursts and other firing tests featuring pressure oscillations of the SVS type. This could be due to

the presence of a large cavity without flow injection in the rear part of the engine.

Acknowledgments

The hot-gas firing tests presented in this paper were performed and financed by ONERA–The French Aerospace Lab (ONERA). They complement research activities carried out within the Research and Technology Program cofinanced by the Centre National d'Etudes Spatiales and ONERA.

References

[1] Dotson, K. W., Koshigoe, S., and Pace, K. K., "Vortex Shedding in a Large Solid Rocket Motor Without Inhibitors at the Segmented Interfaces," *Journal of Propulsion and Power*, Vol. 13, No. 2, 1997, pp. 197–206. doi:10.2514/2.5170

[2] Brown, R. S., Dunlap, R., Young, S. W., and Waugh, R. C., "Vortex Shedding as a Source of Acoustic Energy in Segmented Solid Rockets," *Journal of Spacecraft*, Vol. 18, No. 4, 1981, pp. 312–319. doi:10.2514/3.57822

[3] Blomshield, F. S., and Mathes, H. B., "Pressure Oscillations in Post-Challenger Space Shuttle Redesigned Solid Rocket Motors," *Journal of Propulsion and Power*, Vol. 9, No. 2, 1993, pp. 217–221. doi:10.2514/3.23612

[4] Fabignon, Y., Dupays, J., Avalon, G., Vuillot, F., Lupoglazoff, N., Casalis, G., and Prévost, M., "Instabilities and Pressure Oscillations in Solid Rocket Motors," *Aerospace Science and Technology*, Vol. 7, No. 3, 2003, pp. 191–200. doi:10.1016/S1270-9638(02)01194-X

[5] Anthoine, J., "Solid Propellant Pressure Oscillations," *VKI / STO-AVT-206 Lecture Series on Fluid Dynamics Associated to Launcher Developers*, von Kármán Inst., Rhode-Saint-Genèse, Belgium, April 2013.

[6] Vuillot, F., "Vortex-Shedding Phenomena in Solid Rocket Motors," *Journal of Propulsion and Power*, Vol. 11, No. 4, 1995, pp. 626–639. doi:10.2514/3.23888

[7] Hijlkema, J., Prévost, M, and Casalis, G., "On the Importance of Reduced Scale Ariane 5 P230 Solid Rocket Motor Models in the Comprehension and Prevention of Thrust Oscillations," *CEAS Space Journal*, Vol. 1, No. 4, 2011, pp. 99–107. doi:10.1007/s12567-011-0008-8

[8] Culick, F. E. C., "A Review of Calculations for Unsteady Burning of a Solid Propellant," *AIAA Journal*, Vol. 6, No. 12, 1968, pp. 2241–2255. doi:10.2514/3.4980

[9] Kuentzmann, P., "Combustion Instabilities," *AGARD Lecture Series 180*, AGARD, 1991, pp. 7-1–7-31.

[10] Flandro, G. A., and Jacobs, H. R., "Vortex Generated Sound in Cavities," AIAA Paper 1973-1014, 1973.

[11] Vuillot, F., "Point sur les Recherches Relatives à la Stabilité de Fonctionnement du MPS P230 d'Ariane 5," *Proceedings of the 3ème Colloque R&T CNES/ONERA, Ecoulements Internes en Propulsion Solide*, Ecole Nationale Superieure de Mecanique et d'Aerotechnique, Chatillon-sous-Bagneux, France, 1998.

[12] Taylor, G., "Fluid Flow in Regions Bounded by Porous Surfaces," *Proceedings of the Royal Society of London, Series A: Mathematical and Physical Sciences*, Vol. 234, No. 1199, 1956, pp. 456–475.

[13] Culick, F. E. C., "Rotational Axisymmetric Mean Flow and Damping of Acoustic Waves in a Solid Propellant Rocket," *AIAA Journal*, Vol. 4, No. 8, 1966, pp. 1462–1464. doi:10.2514/3.3709

[14] Price, E. W., "Solid Rocket Combustion Instability—An American Historical Account," *Nonsteady Burning and Combustion Stability of Solid Propellants, Progress in Astronautics and Aeronautics*, Vol. 143, AIAA, Washington, D.C., 1992, pp. 1–16, Chap. 1.

[15] Strand, L. D., and Brown, R. S., "Laboratory Test Methods for Combustion-Stability Properties of Solid Propellants," *Nonsteady Burning and Combustion Stability of Solid Propellants, Progress in Astronautics and Aeronautics*, Vol. 143, AIAA, Washington, D.C., 1992, pp. 689–718, Chap. 17.

[16] Lupoglazoff, N., and Vuillot, F., "Parietal Vortex Shedding as a Cause of Instability for Long Solid Propellant Motors: Numerical Simulations and Comparisons with Firing Tests," AIAA Paper 1996-0761, 1996.

[17] Avalon, G., Ugurtas, B., Grisch, F., and Bresson, A., "Numerical Computations and Visualization Tests of the Flow Inside a Cold Gas Simulation with Characterization of a Parietal Vortex Shedding," AIAA Paper 2000-3387, 2000.

[18] Yagodkin, V. I., "Use of Channels with Porous Walls for Studying Flows Which Occur During Combustion of Solid Propellants," *Proceedings of the 18th International Astronautical Congress*, Vol. 3, International Astronautical Federation, Paris, 1967, pp. 67–79.

[19] Dunlap, R., Blackner, A. M., Waugh, R. C., Brown, R. S., and Willoughby, P. G., "Internal Flow Field Studies in a Simulated Cylindrical Port Rocket Chamber," *Journal of Propulsion and Power*, Vol. 6, No. 6, 1990, pp. 690–704. doi:10.2514/3.23274

[20] Avalon, G., and Josset, Th., "Cold Gas Experiments Applied to the Understanding of Aeroacoustic Phenomena Inside Solid Propellant Boosters," AIAA Paper 2006-5111, 2006.

[21] Flandro, G.A., "Vortex Driving Mechanism in Oscillatory Rocket Flows," *Journal of Propulsion and Power*, Vol. 2, No. 3, 1986, pp. 206–214. doi:10.2514/3.22871

[22] Chedevergne, F., and Casalis, G., "Detailed Analysis of the Thrust Oscillations in Reduced Scale Solid Rocket Motors," AIAA Paper 2006-4424, 2006.

[23] Chedevergne, F., Casalis, G., and Feraille, T., "Biglobal Linear Stability Analysis of the Flow Induced by Wall Injection," *Physics of Fluids*, Vol. 18, No. 1, 2006, Paper 014103. doi:10.1063/1.2160524

[24] Casalis, G., Boyer, G., and Radenac, E., "Some Recent Advances in the Instabilities Occurring in Long Solid Rocket Motors," AIAA Paper 2011-5642, 2011.

[25] Chedevergne, F., Casalis, G., and Majdalani, J., "Direct Numerical Simulation and Biglobal Stability Investigations of the Gaseous Motion in Solid Rocket Motors," *Journal of Fluid Mechanics*, Vol. 706, Sept. 2012, pp. 190–218. doi:10.1017/jfm.2012.245

[26] Gazanion, B., Chedevergne, F., and Casalis, G., "On the Laminar-Turbulent Transition in Injection-Driven Porous Chambers," *Experiments in Fluids*, Vol. 55, No. 1643, 2013. doi:10.1007/s00348-013-1643-y

[27] Anthoine, J., Buchlin, J.-M., and Hirschberg, A., "Effect of Nozzle Cavity on Resonance in Large SRM: Theoretical Modeling," *Journal of Propulsion and Power*, Vol. 18, No. 2, 2002, pp. 304–311. doi:10.2514/2.5935

[28] Anthoine, J., and Lema, M. R., "Passive Control of Pressure Oscillations in Solid Rocket Motors: Cold Flow Experiments," *Journal of Propulsion and Power*, Vol. 25, No. 3, 2009, pp. 792–800. doi:10.2514/1.39794

[29] Prévost, M., Godon, J. C., and Innegraeve, O., "Thrust Oscillations in Reduced Scale Solid Rocket Motors, Part I: Experimental Investigations," AIAA Paper 2005-4003, 2005.

[30] Radenac, E., Fabignon, Y., Casalis, G., and Prévost, M., "Simulation of a Solid Propellant Subscale Motor with a 3-D Protruding Inhibitor," *Space Propulsion Conference*, Association Aeronautique et Astronautique de France, San Sebastian, Spain, May 2010.

[31] Ribéreau, D., Pevergne, T., Le Helley, P., Jacques, L., Prévost, M., and Cesco, N., "Thrust Oscillations Passive Control on Large Solid Rocket Motors," AIAA Paper 2005-4168, 2005.

[32] Germani, T., Mastrangelo, G., Boury, D., Bouvier, F., Fontana, A., Telara, M., Lecoustre, M., and Cesco, N., "Ariane 5 S.R.M. ARTA Firing Tests Program Lesson Learned and Perspectives," AIAA Paper 2005-3790, 2005.

[33] Vetel, J., "Interaction des Structures Pariétales sur le Développement Instationnaire d'Ecoulements Cisaillés en Milieu Confiné—Rôle de l'Injection Différentielle," Ph.D. Thesis, Univ. de Poitiers, Poitiers, France, 2001.

[34] Hilbert, D., "Grundzüge Einer Algemeinen Theorie der Linearen Integralgleichungen," Chelsea Publishing Company, New York, 1953.

[35] Cauty, F., "Non-Intrusive Measurement Techniques Applied to the Hybrid Motor Solid Fuel Degradation," *2nd International Conference on Green Propellants for Space Propulsion*, ESA Publications Division, ESTEC, Noordwijk, The Netherlands, 2004.

[36] David, B., and Badeau, R., "Fast Sequential LS Estimation for Sinusoidal Modeling and Decomposition of Audio Signals," *IEEE Workshop on Applications of Signal Processing to Audio and Acoustics*, IEEE, Piscataway, NJ, Oct. 2007, pp. 211–214.